ADVANCED MATERIALS TECHNOLOGIES
www.advmattechnol.de

Physical Virtualization of a GFET for a Versatile, High-Throughput, and Highly Discriminating Detection of Target Gas Molecules at Room Temperature

*Michele Zanotti, Sonia Freddi, and Luigi Sangaletti**

An e-nose is built on a single graphene field effect transistor (GFET), based on a graphene/Si_3N_4/p-Si stack of layers. Multichannel data acquisition, enabling to mimic the architecture of a sensor array, is achieved by steering the gate potential, thus yielding a virtual array of 2D chemiresistors on a single sensing layer. This setting allows for the detection of volatile compounds with a remarkable discrimination capability, boosted by intensive machine learning analysis and accuracy maximization through the choice of the number of virtual sensors. Sensing of gas phase NH_3 is tested, along with a set of possible interferents, and discrimination of NH_3+NO_2 mixtures is successfully probed. High throughput in terms of sensitivity is achieved by tracking the shift of the minimum of the GFET transfer curve versus NH_3 concentration. With this readout scheme, a 20-fold sensitivity increase over a 5–50 ppm range is registered to the same layer used as a chemiresistor. High discrimination capability is probed by leveraging machine learning algorithms, from principal component analysis (PCA) to Uniform Manifold Approximation and Projection (U-MAP) and, finally, to a Deep Neural Networks (DNN) where input neurons are the virtual sensors created by the gate voltage driving. For the tested case, the DNN maximum accuracy is achieved with 21 virtual sensors.

1. Introduction

Due to their exceptional sensitivity to changes in the surrounding environment, Graphene Field-Effect Transistors (GFETs) is a promising technology for gas sensor based artificial olfaction.[1] GFET-based gas sensors operate on the principle that the electrical properties of graphene are highly sensitive to the presence of gas molecules, which can alter the conductivity of the graphene channel in the transistor [see, e.g., Section 6. in ref. [2], and ref. [3–12]. GFET-based gas sensors can provide real-time monitoring of gas concentrations and are suitable for various applications determined by the current societal priorities and industrial needs, including environmental monitoring, industrial safety, and healthcare.[13] The advantages of GFET-based gas sensors are manifold, including high sensitivity, down to single molecule detection,[3] rapid response times,[14] and the potential for miniaturization, making them attractive for portable and wearable gas sensing devices.

To maintain the sensitivity to a specific target molecule even in the presence of interferent gases, thus increasing the discrimination capabilities, single sensors can be assembled into arrays, usually called electronic noses (e-noses). Depending on the number of sensors employed, it is possible to define two classes of devices: e-noses based on sensor arrays (with a sensor number ≥ 2) and e-noses based on virtual sensor arrays (or single sensor e-noses).[15] In the case of graphene, sensor-array based e-noses have been recently proposed [see, e.g., ref. [16] and ref. [17–20]]. In a sensor-array based e-nose, the combined responses of multiple sensors can be processed to create unique patterns for different odors, improving the accuracy and reliability of odor identification. However, with a sensor-array based e-nose the complexity of device manufacturing may increase, in terms of, e.g., wiring for signal read-out and the electronics for multiplexed data acquisition. On the other hand, because of the presence of the tunable gate channel, GFETs provide more degrees of freedom in the device driving and data readout, as compared to, e.g., chemiresistors. Therefore, they could be regarded as promising devices to proceed with a multifeatured extraction from the response curve

M. Zanotti, S. Freddi, L. Sangaletti
Department of Mathematics and Physics
Università Cattolica del Sacro Cuore
via della Garzetta, 48, BresciaBS 25133, Italy
E-mail: luigi.sangaletti@unicatt.it
M. Zanotti
Department of Chemistry
KU Leuven
Celestijnenlaan 200F, Leuven3001, Belgium
S. Freddi
Institute for Photonics and Nanotechnologies (IFN) – Consiglio Nazionale delle Ricerche (CNR)
L-NESS laboratory
Politecnico di Milano
sede di Como, via Anzani 42, Como22100, Italy

The ORCID identification number(s) for the author(s) of this article can be found under https://doi.org/10.1002/admt.202400985

DOI: 10.1002/admt.202400985

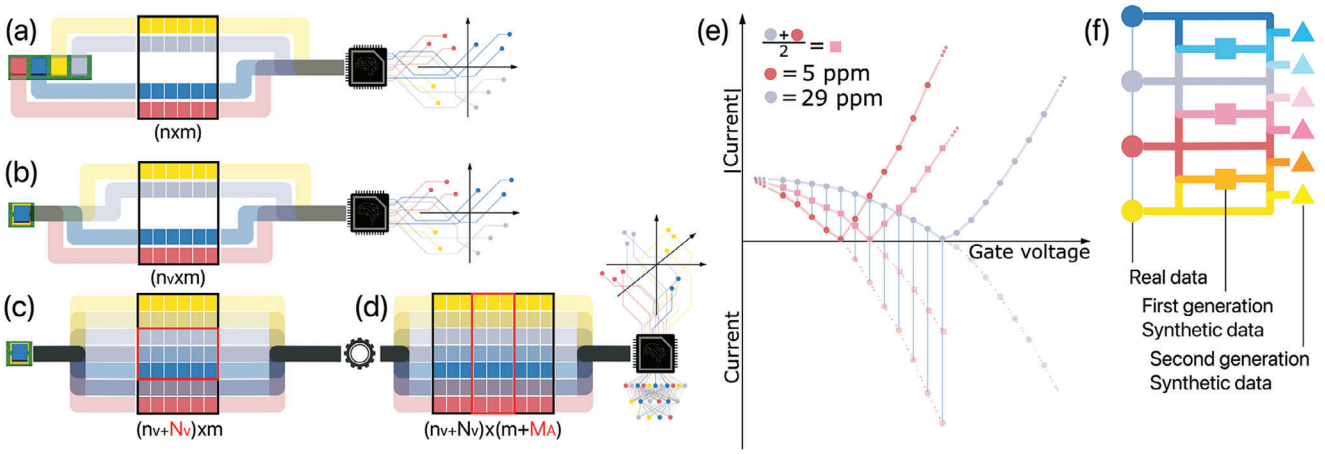

Figure 1. Evolutionary architecture of a single GFET-based e-nose. a–d) depict the various configurations of electronic noses, each representing a distinct stage of evolution. The initial configuration a) represents the traditional architecture commonly employed (n-sensor array that records a set of m gas exposures). The first step of the system evolution is illustrated in b), where sensor virtualization is achieved (n_v virtual sensors array from a single GFET rather than n real sensors in an array). Subsequently, the second step of the system evolution Involves the creation of further virtual sensors in the array (n_V+N_V) and synthetic data generation (m+M_A), as exemplified in d). This technique serves to expand the dataset and facilitates the utilization of diverse machine learning algorithms, such as neural networks. The highlighted rectangular boxes represent the data matrix used to feed the ML algorithm; e) schematics of data generation. For each couple of experimental *I–V* curves, an intermediate curve is generated through a suitable linear combination of corresponding experimental data; f) additional processes in synthetic data production. Circles represent the experimental data, while squares are the first generation of data augmentation and triangles the second generation of data augmentation.

of a single sensor and to apply machine learning algorithms to the analysis of a multi-dimensional parameter space.

The way to use a single sensing layer as an e-nose is based on the possibility of extracting a set of values (features) from, for example, DC channel conductance and transfer curves. The extracted features can then be leveraged by machine learning algorithms to achieve higher discrimination performances. In the case of GFET, this approach was recently applied by Hayasaka et al. to GFET transfer curves, from which four features were extracted.[21] As was proposed for other classes of devices, this idea can be extended to other features that can be acquired during the gas exposure such as the dynamical response curve in the frequency domain in the case of ZnO sensing layers on SiO_2[22] or selected features in a SiC FET dynamical response curve.[23]

In this study, we address the question whether a single GFET can be effectively operated as a virtual electronic nose with an arbitrary number of parameters, thus avoiding the use of several sensors and multiplexing and, at the same time, preserving a simple readout scheme through an effective and scalable driving of the gate. Here the features, rather than being different physical quantities extracted from the response curve, as reported in ref. [21] are determined by steering the gate voltage, thus allowing for the choice of the optimal number of features for a specific target gas dataset. We show that this approach allows for an optimization of sensitivity (20x to ammonia), discrimination, and prediction capabilities.

In detail, we present an evolutionary architecture for a single GFET-based electronic nose, developed on a two-step process. The first step, depicted in **Figure** 1a,c, achieves results comparable to a sensor-array based electronic nose by employing only one graphene field-effect transistor instead of multiple sensors. We refer to this initial stage as "sensor virtualization" because the tuning of the gate voltage enables the creation of a manifold of virtual sensors with distinct "doping" characteristics of the graphene channel. As we will show, the number of virtual sensors can be increased at will to obtain the best accuracy in the classification procedure. This represents a significant breakthrough, albeit accompanied by certain challenges inherited from previous architectures. The second step (Figure 1c,d) is enabled by a proper choice and application of machine learning algorithms. As a limited size of the experimental dataset may restrict the application of numerous machine learning classification algorithms, a protocol for "synthetic data generation" is developed (Figure 1e,f), which enables the applications of data reduction and further classification with a neural network NN in a deep learning approach (DNN). Data reduction was achieved both with Principal Component Analysis (PCA) and Uniform Manifold Approximation and Projection (U-MAP) approaches. The latter serves as a non-linear approach to dimensionality reduction and is particularly useful with noisy, sparse, or data types unsuitable for effective reduction through linear techniques as principal component analysis. U-MAP approaches are virtually missing in e-noses data analysis, but we can show the better performances of U-MAP in data classification. Hence, U-MAP was chosen over PCA for its robustness in handling such complex data structures.

Choosing NH_3 as a testing gas (along with a set of interferents), it will be shown that i) the V_{gate} readout of GFET outperforms (20x signal enhancement) in ammonia detection the chemiresistor readout based on the same sensing layer. ii) discrimination of NH_3 against NO_2, and other interferents (NO_2, acetone, ethanol, IPA, sodium hypochlorite) is dramatically increased.

Here, NH_3 as the target gas molecule has been selected because, in addition to being a benchmark target gas molecule for chemiresistor gas sensors, ammonia monitoring is important in the field of environmental control, healthcare, and food and beverage quality assessment.[24–27]

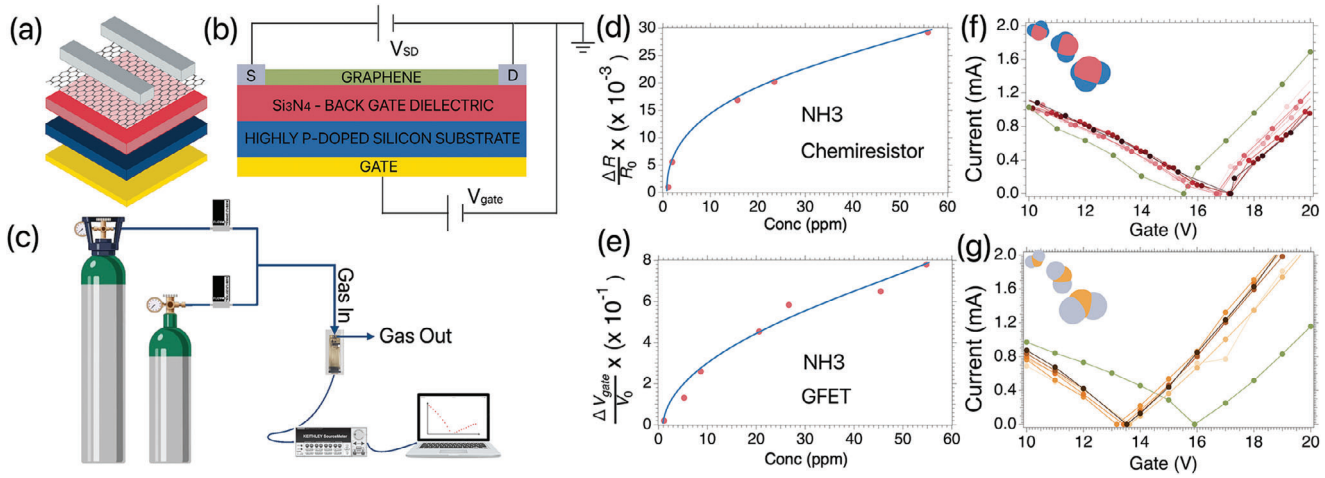

Figure 2. a) Layout of the GFET with all layers vertically stacked. From bottom: gate contact, p-doped silicon wafer, Si_3N_4 dielectric, graphene channel, source and drain electrodes. b) Electrical layout of the GFET with grounding and voltage sources; c) Schematic representation of the gas measurement system, comprising two cylinders housing synthetic air and analytes, respectively, as well as two mass flow controllers, the measurement chamber, and the data acquisition electronics. d) chemiresistor calibration curve for NH_3 detection in the 0–60 ppm range; e) GFET calibration curve for NH_3 detection in the 0–60 ppm range; f) GFET *I–V* curves measured for different concentrations of NH_3. The red curve corresponds to the transfer curve without the analyte, while the shift observed in the transfer curve can be attributed to the doping effect exerted by the analyte; g) GFET *I–V* curves measured for different concentrations of NO_2. In this case, the observed shift occurs in the opposite direction relative to panel (f).

The interferent gases have been selected regarding the applications: indeed, for instance, ethanol has started to be largely exploited in biofuel, but it contributes to ozone formation and increase in air smog,[28] while NO_2 is one of the most common pollutants in the atmosphere. Additionally, all the selected interferents are considered biomarkers for several pathologies, including lung cancer (IPA and ethanol),[29] diabetes (acetone),[30] chronic obstructive pulmonary disease (NO_2),[25] and cystic fibrosis (sodium hypochlorite).[31]

2. Results

2.1. Sensing Layer and GFET Characterization

Material characterization has been carried out through Raman spectroscopy, atomic force microscopy (AFM), and X-ray photoemission spectroscopy (XPS). Data are shown in Figure S1 (Supporting Information). Raman spectra taken over different regions of the sensing layer present the G and 2D bands expected for graphene. The defect band at ≈1350 cm^{-1} displays a negligible contribution. The ratio between the G and 2D bands intensity is I_G/I_{2D} = 0.47. This finding, along with the weak contribution from the D band, is indicative of a defect-free monolayer graphene.[32] A representative Raman spectrum collected from the graphene layer is shown in Figure S1a (Supporting Information). AFM scanning resulted in a rather uniform layer with a roughness of ≈0.5 nm. An AFM scan across a 3μm x 3μm area is shown in Figure S1b (Supporting Information). Finally, XPS spectra have been collected from the as-received layer before and after a mild annealing in the ultra-high vacuum chamber of the XPS spectrometer (Figure S1, Supporting Information). Data in Figure S1c (Supporting Information) were collected from the as-received graphene surface exposed to the laboratory atmosphere. This is the typical condition of the graphene layer before exposure to analytes. In particular, Figure S1c (Supporting Information) shows the C 1s XPS core level. After a fitting of the C 1s spectral weight with Voigt line-shape function, several carbon related features are detectable. The one at the lowest binding energy (BE) is ascribed to the C—C bond in the graphene layer, while the other features are ascribed to C—O, C═O, and O—C═O bonds.[20] After mild annealing (150 °C) in ultra-high vacuum conditions (Figure S1d, Supporting Information) most of the high binding energy features either disappear or are strongly quenched. This suggests that they can be ascribed to adventitious molecules physiosorbed when the layer is exposed to the laboratory air.

The sensing device, composed of a stack of Si, Si_3N_4, and graphene layers (**Figure 2a**) was connected to two voltage sources (V_{gate} and V_{SD}) according to the wiring scheme of Figure 2b and then inserted into a chamber where it was exposed to analyte gas molecules (Figure 2c). Sensitivity to ammonia and selected interfering gases was determined in a single chemiresistor configuration, which sets a ground level for further measurements. In this respect, the chemiresistor can be regarded as a GFET with V_{gate} = 0 V. A typical dynamical response of the chemiresistor upon NH_3 exposure is shown in Figure S2 (Supporting Information).

From this kind of data, the sensor response time τ_{resp} can be extracted as τ_{resp} = 150 ± 15 s. This time is defined as the time required to register a signal increase from 0 to 90% of the maximum value. Likewise, the recovery time τ_{rec} was estimated to be τ_{rec} = 75 ± 20 min (from 100% to 10% of the maximum signal). This time is much longer than the response time, but it is a typical time for sensors operating at room temperature.

From this preliminary set of measurements on ammonia, a calibration curve of the chemiresistor was determined (Figure 2d), where the relative change $(R-R_0)/R_0$ of sample resistance versus NH_3 concentration was tracked in the 0–60 ppm NH_3 range. Here R_0 is the baseline resistance before gas

exposure, while R is the maximum resistance value registered during each exposure to NH_3. From the response to NH_3 (an electron-donor molecule), it is possible to infer that the present graphene layer has a *p*-type behavior (i.e., holes are the majority carriers). Therefore, when our GFET is exposed to gas that donates electrons, the I_{SD} versus V_{gate} transfer curve, which represents the relationship between the source-drain current I_{SD} and gate voltage, is expected to undergo a rightward shift, given the grounding and voltage polarity scheme of Figure 2b. The shift (Figure 2f) arises from an increase in the electron concentration within the graphene channel, resulting in a reduction in the hole concentration. The shift of the V_{gate} leading to $I_{SD} = 0$ was also tracked versus NH_3 concentration in the 0–60 ppm range, resulting in the calibration curve of Figure 2e, where $(V_{gate} - V_{gate,0})/V_{gate,0}$ is shown versus $[NH_3]$. Here $V_{gate,0}$ is the gate voltage yielding $I_{SD} = 0$ (i.e., the Dirac point voltage of the graphene layer) before gas exposure, while V_{gate} is the Dirac point voltage registered during each exposure to NH_3. A comparison between the two calibration curves (Figure 2d,e) clearly shows that when operated as a GFET the sensing layer displays a response to ammonia in the 0–60 ppm concentration range that is ≈20x larger than when operated as a simple chemiresistor, thus displaying the first advantage of driving the device as a GFET.

To the chemiresistor readout, for the GFET a different approach for data collection is adopted, and therefore the dynamical response changes. The chamber needs to reach a saturation condition before starting the V_{GATE} scanning. Here time scales are mainly determined by the fluid dynamics of the chamber. This is the reason simulations on the chamber filling are displayed in the Supporting Information (Figure S3, Supporting Information). A gas exposure in the GFET configuration takes 4 s to fill the chamber, the V_{GATE} scan from 0 to 60 volts takes 30 s (averaging 100 I_{SD} values for each V_{GATE} value), and finally, the chamber is purged in 4 s. Therefore, each gas exposure takes no more than 38 s. This time can be reduced by reducing the chamber volume, averaging over a minor set of I_{SD} values for each V_{GATE}, or reducing the V_{GATE} range. Anyway, the time required for the overall process in the GFET configuration is shorter than the recovery time determined by the chemiresistive behavior, which is therefore the longest timescale in the process. In principle, this recovery time can be reduced by operating the system at higher temperatures, induced by, e.g., UV irradiation, pulsed heating, or a pulsed I_{SD} during the recovery phase.

It is important to note that, to find the best conditions for NH_3 detection, several tests were carried out to determine the optimal voltage (V_{SD}) to be applied between the source and drain contacts. The results of these tests are shown as transfer curves in Figure S4 (Supporting Information). The V_{SD} voltage was varied in the 0.3–2.1 V voltage range, while V_{GATE} was scanned from 0 to 60 V. In Figure S4 (Supporting Information), the red lines depict measurements conducted without the target gas, whereas the blue lines represent measurements obtained during exposure to NH_3 (55 ppm). Notably, the figure reveals that the current-voltage (*I*–*V*) curve becomes sharper, and the left branch of the curve displays higher current values as V_{SD} increases. Furthermore, a higher voltage between the source and drain requires a correspondingly higher gate voltage to observe the *I*–*V* curve during NH_3 exposure. Another crucial consideration in selecting the gate voltage range pertains to the data analysis. It is advantageous to incorporate a large number of V_{GATE} values because this corresponds to a larger set of virtual sensors that can be used for analyte classification. Based on these measurements, a V_{SD} of 1.1 V and V_{gate} in the 0–60 V range resulted to be the most suitable for the present study.

If the transfer function of p-doped GFET gas sensors exhibits a rightward shift when exposed to reducing gases (Figure 2f), a leftward shift is expected when exposed to oxidizing gases, which is indeed observed in Figure 2g, resulting from a set of exposures to NO_2. Calibration curves obtained after exposure to NO_2 in the chemiresistive and GFET readout are shown in Figures S5a,b (Supporting Information), respectively. Also, in this case, the GFET readout displays a larger sensitivity than the chemiresistor readout in the same range of NO_2 concentration.

The stability of the sensing characteristics has been checked by collecting new I_{SD}–V_{GATE} curves 120 days after the earlier measurements, with NH_3 concentrations ranging from 0 to 63 ppm. Data are shown in Figure S6 (Supporting Information). As can be noticed, the Dirac points are found in the correct sequence (i.e., the Dirac points scale with $[NH_3]$) irrespectively of the 120 days time lag among them. Furthermore, the $V_{GATE} = 0$ curves collected at t = 0 and t = 120 days are superimposed.

Also in the case of graphene,[33] water vapor is recognized as an interferent in gas sensing in ambient air. In some cases, the presence of water can enhance the sensitivity to ammonia of nanostructured carbon-based sensing layers, as was demonstrated for CNTs in ref. [34] In the present case, I_{SD}-V_{GATE} curves collected at different R.H. values show that the R.H. increase determines a shift of the Dirac point both in air without ammonia and in air with 43 ppm of ammonia (Figure S7 Supporting Information). Consistently with ref. [33] the largest shift of the Dirac point when ammonia concentration increases from 0 pm to 43 ppm is registered for larger (R.H. = 40%) humidity values, thus showing that H_2O effects cannot be neglected in the sensing process in ambient air. In our case, R.H. values were monitored for each exposure with the aim to keep track of these effects.

2.2. E-Nose from GFET Virtualization

The virtual e-nose is developed by using a set of 61 V_{gate} values in the 0–60 V range to mimic the behavior of a sensor array. In this novel architecture (Figure 1b,c) only one sensor is employed to build the e-nose. Notably, this sensor operates in a FET configuration, wherein the channel doping is controlled by the applied gate voltage. Conceptually, one can visualize an array of "virtual sensors", where each virtual sensor corresponds to a predetermined gate voltage setting. Rather than solely capturing the sensor signals, the focus shifts toward recording the transfer curve of the FET sensor. Each data point on this curve corresponds to a specific gate voltage, allowing for the creation of a dataset in the form of a table where columns represent the I_{SD} current values obtained by scanning the gate voltage and each row represents one of the gas exposures. This dataset serves as the input for subsequent PCA to extract informative features. Remarkably, the outcomes obtained using this modified architecture closely resemble those of the traditional electronic nose, with the added advantage of flexibility in choosing the number of (virtual) sensors to be used.

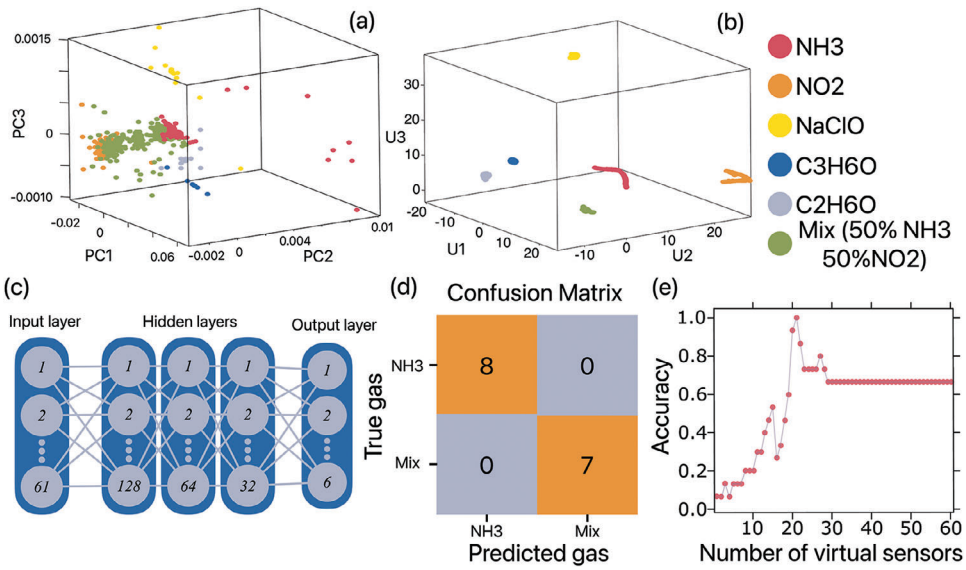

Figure 3. Results of a) PCA and b) U-MAP. c) Features of the Neural Network (3 hidden layers with 128-64-32 cells). d) Confusion matrix for the classification obtained using the neural network with 21 input neurons, corresponding to the maximum accuracy. e) Accuracy of DNN classification versus number of virtual sensors.

Following the data analysis usually adopted for e-noses,[35] we proceeded with data reduction through PCA analysis. PCA aims to identify the principal components that capture the maximum variance in the dataset, thereby enabling effective visualization and discrimination of patterns. In this analysis, the initial dataset consisted of 61 virtual sensors representing distinct gate voltages, with a total of 37 exposures to several analytes in the gas phase. It is important to note that in PCA it is generally not advisable to have more columns than rows in the dataset. When the number of columns exceeds the number of rows, the dataset becomes rank-deficient, impeding the accurate estimation of the covariance matrix and the subsequent extraction of meaningful principal components. To address this limitation a subset of 28 columns was used to maintain a balanced dataset. In this approach, a systematic column selection process was implemented, alternating between retaining and removing a single column. The results shown in Figure S8 (Supporting Information) represent the best discrimination obtained from all possible selections of a set of 28 columns (i.e., virtual sensors) out of 61. Each plot represents a combination of 2 among PC1, PC2, and PC3 components The best outcome among these selections is defined as the one that accounted for the largest variance in the first three (i.e., PC1, PC2, and PC3) principal components. However, while optimizing classification, the reduction of features may lead to information loss. Therefore, assuming that the main limitation from the point of view of data collection is the number of events (here the number of exposures to gas) one is forced to seek alternative strategies.

2.3. Data Augmentation to Enable More Efficient M–L Tools

To overcome limitations from the previous PCA analysis, the second step in our evolutionary architecture has been introduced. This step introduces an additional component between the dataset creation and data analysis stages, known as data augmentation. Data augmentation plays a central role in expanding the available dataset by generating artificial data based on the experimentally collected samples. The process of data augmentation is summarized in Figure 1d,e.

Let us consider the exposure to gases depicted in Figure 2f,g, as an example. Notably, as the gas concentration increases, the transfer curve progressively shifts relative to the transfer curve acquired in ambient air. Leveraging on this observation, the proposed algorithm cyclically combines pairs of real measurements, generating intermediate synthetic measurements through linear interpolation while incorporating also additional random noise (i.e. jitter, Figure 1e). The newly generated data points are then incorporated into the pool of real measurements and can be selected in subsequent cycles (Figure 1d). The algorithm allows for the specification of the desired number of generated data points. In this study, 500 data points were generated for each gas, as this quantity provides a reasonable dataset size for the application of artificial intelligence algorithms.

The outcomes of the second step are visually presented in **Figure** 3a–d, which show the PCA and U-MAP results, the DNN scheme, and the confusion matrix, respectively.

To PCA (Figure 3a), the U-MAP visualization (Figure 3b) demonstrates the effectiveness of the data generation approach in creating more distinct and well-separated clusters. The confusion matrix (Figure 3d), based on the outcome of the DNN (Figure 3c), offers a comprehensive assessment of the classification performance. Here the best performing DNN was based on a cascade of three hidden layers with 128, 64, and 32 neurons, respectively, with an input layer including up to 61 neurons, and a final output layer with 6 neurons for the discrimination of five analytes and one NH_3-NO_2 mixture. The input layer thus contains the virtual sensors, while the neurons in the output layer represent the different analytes, or mixtures, to be identified. The output layer utilizes a *softmax* activation function, which converts the output

into a probabilistic distribution that assigns a probability value to each class label, allowing for accurate classification and prediction.

Before the data generation process, the dataset was divided into training and testing subsets. The test dataset includes seven measurements acquired with the NH_3 and NO_2 mixtures and eight measurements for NH_3 at different concentrations and variable R.H. conditions (i.e., between 4% and 40%). As the data generation has been performed before training ML models, variability in datasets due to new measurements can be accounted for by scheduling periodical re-training with new real data from a specific analyte and known concentration.

The data generation process resulted in a training dataset of 3000 rows (500 rows for each of the 5 analytes and 500 extra rows for a NO_2-NH_3 mixture) and 61 columns (i.e., virtual sensors). Due to the choice to add jitter in data augmentation. U-MAP is preferred over PCA as the latter, being based on covariance, would overestimate this noise in data reduction. Furthermore, an additional step in the data generation process was introduced to enable the recognition of gas mixtures and included in the U-MAP classification/clusterization. To achieve this, a virtual cluster of measurements is created by linearly combining the clusters of two analytes. Therefore, a virtual cluster representing the mixture of NH_3 and NO_2 was generated. Starting with two clusters, each consisting of 500 measurements, a linear combination of data was considered, still incorporating random noise (jitter). This process results in the generation of an additional cluster of 500 synthetic data, corresponding to the NH_3 and NO_2 mixture. The specific mixture in this study comprises a 50%–50% NH_3-NO_2 composition. However, by adjusting the weights in the linear combination, the approach can be adapted to detect other gas mixtures. This flexibility allows for the customization of the approach based on the specific application requirements.

The U-MAP visualization, as depicted in Figure 3b, demonstrates the efficacy of the data generation process by revealing distinct and well-separated clusters. The expanded dataset facilitated accurate predictions for the unseen testing data. This is exemplified in the confusion matrix, illustrated in Figure 3d, which showcases the neural network ability to correctly predict all the provided testing dataset samples.

3. Discussion

The results presented in the calibration curves (Figure 2d,e) clearly show the starting advantage of using a GFET readout scheme to a conventional chemiresistor for NH_3 detection. The same holds for NO_2 detection, as displayed in Figure S5 (Supporting Information).

While benchmarking is feasible among single chemiresistors (see, e.g., Table 1 in ref. [20] for NO_2, and Figure 7 of ref. [36] for NH_3), provided that the measurement conditions are properly specified, benchmarking among e-noses strongly depends on the e-nose architecture (real or virtual sensors, number of sensors, measured physical quantity, data analysis method, the definition of accuracy in discrimination) and therefore it is usually difficult to be carried out unless all devices are tested at once on a common test-rig or a specific method for output comparison is defined.[37] Therefore, the use of our readout (i.e., $(V_{gate} - V_{gate,0})/V_{gate,0}$) provides a remarkable sensitivity enhancement to the chemiresistor based on the same sensing layer under identical test conditions. These data have been included in Figure S9 (Supporting Information), where the present device is compared to graphene based chemiresistors for ammonia detection, and in Figure S10 (Supporting Information) for the NO_2 detection. Finally, a list of graphene based e-noses is reported in **Table 1**,[21,38–44] where for each device several features are detailed. As can be observed, a variety of sensing materials have been so far, along with a quite different number of sensors in each e-nose, and different machine-learning methods for data analysis and classification. Accuracy in classification can range from 85% to 100%.

A 20x enhancement of the sensitivity to ammonia is a remarkable result that confirms the potential of GFET in gas sensing. Though this result is potentially common to all GFETs, feature extraction depends on the choice of specific strategies that are, in turn, determined by the readout electronics and data preprocessing. For example, Hayasaka et al. have recently proposed to use a GFET as an e-nose for water, methanol, and ethanol sensing.[21] Their analysis was based on a 4D space of output vectors built with the readout of the electron mobility (μ_e), the carrier concentration (n); the hole mobility (μ_h), and the ratio of the residual carrier concentration to the charged impurity concentration (n^*/n_{imp}). This approach represents one possibility of multi-feature extraction of information from a single sensor. The carrier concentration requires a 4-probe measurement of the voltage across the graphene channel, which to some extent complicates the readout electronics. Furthermore, two of these features, rather than being directly measured, require additional data processing (curve fitting of the transfer curve branches) before being available for machine-learning data treatment. Finally, to illustrate that the accuracy of gas classification could be further improved with more dimensions, a dimension increase of the feature space from 4D to 8D was achieved by introducing a second GFET.

Our e-nose scheme couples a simple electronic readout (I_{SD} vs V_{GATE}) with the possibility to directly measure, without any data pre-processing, an arbitrarily large number of features. This number can be chosen to maximize the accuracy in discrimination, as shown in Figure 3e, where the DNN accuracy is measured by spanning the number of virtual sensors (i.e., features) between 0 and 60. As can be seen, the best result can be obtained with 21 features, a number that is not yet limited by the hardware, which is capable to deal with 60 features (virtual sensors), at least.

As shown in the U-MAP results (Figure 3b), the sensor already displays a sensitivity to multiple analytes and it is able to distinguish the mix between NO_2 and NH_3 (50–50%). The clustering of points in the U-MAP also enables to assess the relative composition of the gas mixture. Indeed, we explored other NO_2-NH_3 mixtures ranging from 0–100% to 100–0%. The mixture's relative composition can be tracked along the path connecting the clusters of the two pure substances. Results are displayed in Figure S11 (Supporting Information).

In real applications, the inhomogeneity of the data set cannot be avoided. Data could be collected over a time range of several weeks or months, and environmental conditions, such as relative humidity, may change over this time range. In this regard, it is crucial to emphasize the remarkable performance of the neural network in classifying data that significantly deviated from the training data. Indeed, the NH_3 measurements of the

Table 1. List of e-noses based on G-FETs and their main features: sensing material, number of sensors, mixtures detection, machine-learning data analysis methods, accuracy in prediction.[21,38–44] LDA=linear discriminant analysis; PLS=partial least squares regression; SVM=supported vector machine; CNN=convolutional neural network; ANN=artificial neural network.

Sensing material	# sensors	Tested gases	Mixtures	Analysis technique	The best accuracy obtained in the classification	Refs.
graphene and MXene composites	8	Acetone, Ethanol, Methanol, 2-propanol	Yes	PCA, LDA, PLS	95.8% single gases; 85% mixtures	[38]
DNA-functionalized graphene	7	NH_3, H_2S, NO	Yes	PCA, SVM, CNN	98%	[39]
Receptor-functionalized graphene	36	EtOH, MEK; Hex, Octa, Octe, Toluene	No	Random forest classification	89%	[40]
thermally reduced graphene oxide	16	Ethanol, Isopropanol, Water, Methanol	No	ANN	–	[41]
Pt/WO3/G, Pd/WO3/GO, WO3/GO	3	Acetone, simulated exhaled breath	Yes	LDA, PLS, ANN	99.1%	[42]
ALD-RuO_2-GFET	1 sensing layer, 4 virtual sensors	Ethanol, methanol, water	No	ANN	100%	[21]
Peptide-Graphene	3	Limonene, Methyl salicylate, menthol	No	PCA	–	[43]
GO, Pd/WO_3/GO, Au/WO_3/GO, WO_3/GO, TiO_2/GO	5	Acetone, Xylene, Methanol, n-pentane, ethanol, formaldehyde	No	LDA, SVM	92.86%	[44]
Graphene	1 sensing layer, up to 61 virtual sensors	Ammonia, Nitrogen dioxide, ethanol, acetone, sodium hypochlorite	yes	PCA; U-MAP; DNN	100%	Present work

testing dataset were acquired in two distinct sets to assess the long-term stability and reproducibility of the sensor (Table S1, Supporting Information). The second set of measurements was taken 4 months after the initial set, introducing a temporal dimension to the dataset. In contrast, for the gas mixture, the training dataset comprised solely synthetic data and was then tested against real exposures to 50%–50% NH_3+NO_2 gas mixtures.

It is important to highlight the variation in humidity levels between the different measurement sets. Specifically, during the acquisition campaign for the second set, half of the measurements were conducted under different humidity conditions compared to the first set. The first set and the initial half of the second set were exposed to a humidity level of 4%, while the latter half of the second set had a humidity level of 40%. The eight measurements for NH_3 included in the test dataset were all taken from the second set of measurements. These choices were considered to assess the long-term stability and performance of the sensor under different conditions, including potential variations over time. Indeed, by incorporating the NH_3 measurements exclusively from the second set, the analysis accounted for any temporal effects, thus providing a more comprehensive evaluation of the proposed methodology ability to accurately predict NH_3 concentrations in real-world scenarios.

Finally, we outline the sensing mechanism which is determined by the interplay between a chemiresistive behavior and the GFET properties. The basic mechanism of gas sensing involves a change in the Fermi level energy and therefore an increase or decrease of the charge carrier density at E_F.[45] This picture is consistent with the finding for our device in the chemiresistive configuration. The GFET configuration further allows for a fine-tuning of the E_F position by steering V_{GATE} to upshift or downshift the Fermi level. In this way, an enhancement in selectivity is available which depends on the combination of V_{GATE} (positive or negative), Gr-layer doping (*p*-type or *n*-type), and analytes properties (reducing vs oxidizing behavior)[46] In our case the graphene layer results to be *p*-type. Interaction with ammonia determines an upward shift of the Fermi level, still preserving the *p*-type doping, as resistivity increases. The application of a potential to the Si back gate determines the polarization of the graphene layer. Depending on the gate polarity, the Fermi level position can be further steered. In addition to the effects related to the Fermi level position, the resistivity of the graphene layer can be determined by the local potential perturbation due to molecule adsorption.[47] Depending on the kind of adsorbed molecules, the scattering due to these local perturbations can overcome even an increase of conductivity, as recently observed for H_2O absorption on holey C-xy graphene.[33] Thus, charge carrier mobility and density appear to be intertwined, so the transport properties are therefore determined by a combination of Fermi level position and scattering processes produced by gas molecule adsorption.[21]

4. Conclusion

There is no universal sensor system that can cope with all gas or vapor analysis problems. Instead, there is a need to employ flexible enough sensor systems that are appropriate to specific applications. We demonstrate that the physical virtualization of our GFET can provide the flexibility required to maximize the discrimination capability in the benchmarking case of NH_3 detection and possible interfering gases. Our GFET outperforms in

ammonia detection the chemiresistor based on the same sensing layer and allows for the optimization of discrimination capabilities through a proper selection of the number of virtual sensors that contribute to the e-nose response. The present GFET is operated at room temperature and therefore, in addition to reducing power consumption, it enables future application in wearable devices. Widespread use of these devices will be made possible by a limited number of electrical contacts to have an electronics readout as simple as possible, and an arbitrarily large feature data set on a single GFET to enable versatility without replicating the device to increase the number of features. The simple steering and readout scheme proposed in the present study reduces the complexity of electronic readout and paves the way for the implementation of the sensor at the microelectronic scale. GFET readout protocol ensures increased sensitivity, while multi-feature extraction allows for high discrimination through U-MAP data analysis and training and testing of an optimized DNN.

5. Experimental Section

GFET Characteristics: The graphene field-effect transistors (GFET) used in this study had been purchased by Graphenea (San Sebastian, Spain) and they are fabricated on a 700 µm thick p-doped Si substrate that directly interfaces with the gate contact. An insulating 150 nm-thick layer of Si_3N_4 had been grown on the Si wafer and, finally, the source-drain channel of the GFETs encompasses a monolayer of graphene synthesized by chemical vapor deposition (CVD) and transferred on the Si_3N_4 layer. All graphene layers tested in the present study were cross-checked by micro-Raman mapping (Renishaw InVia confocal Raman microscope), AFM (Park NX10), and XPS (Scienta R3000). Among all layers, the one chosen for GFET measurements was selected on the basis of best performances as chemiresistor in a batch of 8, nominally identical, samples. Raman data were collected with a Renishaw micro Raman spectrometer equipped with an 1800 l/mm grating and a He-Ne laser with a power of 5 mW at the sample. The laser beam was focussed with a 100x microscope objective. AFM images had been acquired with a Park NX 10 AFM system in a noncontact mode in an air–solid interface with a tip operating at a resonance frequency of ≈300 kHz. All of the image processing had been performed using the Gwyddion software. XPS data were collected in ultra-high vacuum conditions (base pressure = 3×10^{-10} mbar) with a properly calibrated[48] Scienta R3000 electron analyzer and the Al Ka line of a twin anode X-ray source. The overall energy resolution of the XPS probe was set at 0.9 eV.

Figure 2a shows the layered structure of the sample. Silver paint was employed for the source and drained contacts, while the gate contact was a gold film deposited on a printed circuit board (PCB). Figure 2b shows a schematic image of the PCB used for the connection of the sample to the GFET driving and read-out electronics.

The gas measurement setup, shown in Figure 2c, includes two mass flow controllers that link the chamber to distinct gas cylinders. One cylinder contained synthetic air, while the other contained the target gas (purchased and certified by SIAD S.p.a., Bergamo, Italy). The chamber remained sealed throughout the measurements. The experimental procedure initiated with the introduction of synthetic air, allowing the sensor signal to stabilize. Subsequently, the flow of synthetic air ceases, and the target gas was introduced for testing purposes. Once the target gas measurements were completed, synthetic air was reintroduced to purge any residual gas particles from the chamber via the discharge tube. Synthetic air was also used to dilute the target gas concentrations. All the measurements were acquired at room temperature. The chamber volume was 50 cm^3, and filling with the selected gas concentration was achieved in less than 4 s. After filling, the GFET transfer curve was acquired in ≈5 s. Chamber design and dynamics of chamber filling were assessed through the Comsol package (Figure S3, Supporting Information).

All gas exposures and generated datasets are listed in Table S1 (Supporting Information).

Electronics and Data Readout Devices: A Keithley nanoamperometer (model 2634B) was employed for data acquisition purposes. Control of the device and automation of the data acquisition process was facilitated through a Python program developed for this purpose using the Pylab library. The voltage between the source and drain terminals was maintained at a constant value of 1.1 V throughout the experimental procedure. Meanwhile, the gate voltage was systematically varied from 0 to 60 V in increments of 1 V. These parameter settings were established following preliminary investigations into the device response under different voltage conditions, as documented in the Supporting Information. At each increment of the gate voltage, the current passing through the source-drain terminals was averaged over a duration of 0.5 s, with a sampling rate of 200 Hz.

Data Treatment and Machine-Learning Based Analysis: Data had been organized in a matrix where the columns were defined by the different gate voltages and the rows by each exposure to target molecules in the gas phase. Data classification and discrimination were achieved first by PCA and then by U-MAP analysis. Results from these approaches were used for training and testing through deep neural networks (DNN) aimed to classify the outcomes of unknown gas or gas mixture measurements. All algorithms were written using ScikitLearn and Tensorflow Python libraries.

The best configuration of the NN (128,64,32) was achieved through a grid search. For each model, the accuracy was evaluated referring to the confusion matrix. Progression through the hidden layers of the NN was achieved by considering an optimized combination of Linear, Relu, and softMax functions.[49,50] As kernel regularizer we adopted the L2 regularization with a strength set at 0.01. Optimization was achieved with the Adam algorithm, considering a categorical loss function. For the fitting of the model, 100 epoches were considered.[51,52]

Supporting Information

Supporting Information is available from the Wiley Online Library or from the author.

Acknowledgements

M.Z. acknowledges support of the Università Cattolica del Sacro Cuore - KU Leuven Joint PhD Project within the School of Doctorate in Science (2022-23).

Open access publishing facilitated by Universita Cattolica del Sacro Cuore, as part of the Wiley - CRUI-CARE agreement.

Conflict of Interest

The authors declare no conflict of interest.

Data Availability Statement

The data that support the findings of this study are available from the corresponding author upon reasonable request.

Keywords

chemiresistors, e-noses, GFET, machine learning, NH3, U-MAP

Received: June 20, 2024
Revised: August 22, 2024
Published online:

[1] H. K. Patel, *The Electronic Nose: Artificial Olfaction Technology*, Springer, New Delhi **2014**.
[2] A. Paghi, S. Mariani, G. Barillaro, *Small* **2023**, *19*, 2206100.
[3] F. Schedin, A. K. Geim, S. V. Morozov, E. W. Hill, P. Blake, M. I. Katsnelson, K. S. Novoselov, *Nat. Mater.* **2007**, *6*, 652.
[4] X. Yan, Y. Wu, R. Li, C. Shi, R. Moro, Y. Ma, L. Ma, *A. C. S. Omega* **2019**, *4*, 14179.
[5] T. Ikuta, T. Tamaki, H. Masai, R. Nakanishi, K. Endo, J. Terao, K. Maehashi, *Nanoscale Adv* **2021**, *3*, 5793.
[6] G. Lu, L. E. Ocola, J. Chen, *Appl. Phys. Lett.* **2009**, *94*, 083111.
[7] M. Gautam, A. H. Jayatissa, *J. Appl. Phys.* **2012**, *112*, 064304.
[8] P. L. Levesque, S. S. Sabri, C. M. Aguirre, J. Guillemette, M. Siaj, P. Desjardins, T. Szkopek, R. Martel, *Nano Lett.* **2011**, *11*, 132.
[9] B. Kumar, K. Min, M. Bashirzadeh, A. Barati Farimani, M.-H. Bae, D. Estrada, Y. D. Kim, P. Yasaei, Y. D. Park, E. Pop, N. R. Aluru, A. Salehi-Khojin, *Nano Lett.* **2013**, *13*, 1962.
[10] Y. Liu, H. Liu, Y. Chu, Y. Cui, T. Hayasaka, V. Dasaka, L. Nguyen, L. Lin, *Adv. Mater. Interfaces.* **2018**, *5*, 1701640.
[11] S. Masoumi, H. Hajghassem, *Sens. Rev.* **2019**, *39*, 819.
[12] H. Vedala, D. C. Sorescu, G. P. Kotchey, A. Star, *Nano Lett.* **2011**, *11*, 2342.
[13] A. Milone, A. G. Monteduro, S. Rizzato, A. Leo, C. Di Natale, S. S. Kim, G. Maruccio, *Adv. Sustain. Syst.* **2023**, *7*, 2200083.
[14] M. Galvani, S. Freddi, L. Sangaletti, *Sensors* **2024**, *24*, 584.
[15] L. Cheng, Q.-H. Meng, A. J. Lilienthal, P.-F. Qi, *Meas. Sci. Technol.* **2021**, *32*, 062002.
[16] A. Parichenko, S. Huang, J. Pang, B. Ibarlucea, G. Cuniberti, *TrAC Trends in Analytical Chemistry* **2023**, *166*, 117185.
[17] B. Liu, Y. Huang, K. W. L. Kam, W.-F. Cheung, N. Zhao, B. Zheng, *Biosens. Bioelectron: X* **2019**, *1*, 100016.
[18] S. Freddi, C. Marzuoli, S. Pagliara, G. Drera, L. Sangaletti, *RSC Adv.* **2023**, *13*, 251.
[19] N. S. S. Capman, X. V. Zhen, J. T. Nelson, V. R. Saran Kumar Chaganti, R. C. Finc, M. J. Lyden, T. L. Williams, M. Freking, G. J. Sherwood, P. Bühlmann, C. J. Hogan, S. J. Koester, *ACS Nano* **2022**, *16*, 19567.
[20] S. Freddi, M. C. R. Gonzalez, A. Casotto, L. Sangaletti, S. D. Feyter, *Chem. Eur. J.* **2023**, *29*, 202302154.
[21] T. Hayasaka, A. Lin, V. C. Copa, L. P. Lopez Jr., R. A. Loberternos, L. I. M. Ballesteros, Y. Kubota, Y. Liu, A. A. Salvador, L. Lin, *Microsystems & Nanoengineering* **2020**, *6*, 50.
[22] V. Dobrokhotov, A. Larin, D. Sowell, *Sensors* **2013**, *13*, 9016.
[23] G. Domènech-Gil, D. Puglisi, *Sensors* **2022**, *22*, 7340.
[24] M. Chiesa, F. Rigoni, M. Paderno, P. Borghetti, G. Gagliotti, M. Bertoni, A. Ballarin Denti, L. Schiavina, A. Goldoni, L. Sangaletti, *J. Environ. Monit.* **2012**, *14*, 1565.
[25] S. Freddi, A. V. Emelianov, I. I. Bobrinetskiy, G. Drera, S. Pagliara, D. S. Kopylova, M. Chiesa, G. Santini, N. Mores, U. Moscato, A. G. Nasibulin, P. Montuschi, L. Sangaletti, *Adv. Healthcare Mater.* **2020**, *9*, 2000377.
[26] N. T. Brannelly, J. P. Hamilton-Shield, A. J. Killard, *Crit. Rev. Anal. Chem.* **2016**, *46*, 490.
[27] W. Zhang, D.-W. Sun, J. Ma, Z. Wang, A. Qin, B. Z. Tang, *Food Chem.* **2023**, *418*, 135929.
[28] J. D. Willey, G. B. Avery, J. D. Felix, R. J. Kieber, R. N. Mead, M. S. Shimizu, *npj Clim. Atmos. Sci.* **2019**, *2*, 3.
[29] S. Nag, A. Sachan, M. Castro, V. Choudhary, J. F. Feller, *J. Mater. Chem. B* **2017**, *5*, 348.
[30] G.-T. Fan, C.-L. Yang, C.-H. Lin, C.-C. Chen, C.-H. Shih, *Talanta* **2014**, *120*, 386.
[31] A. Zacharasiewicz, N. Wilson, C. Lex, A. Li, M. Kemp, J. Donovan, J. Hooper, S. A. Kharitonov, A. Bush, *Pediatr. Pulmonol.* **2004**, *37*, 273.
[32] A. C. Ferrari, *Solid State Commun.* **2007**, *143*, 47.
[33] M. K. Rabchinskii, V. V. Sysoev, O. E. Glukhova, M. Brzhezinskaya, D. Y. Stolyarova, A. S. Varezhnikov, M. A. Solomatin, P. V. Barkov, D. A. Kirilenko, S. I. Pavlov, M. V. Baidakova, V. V. Shnitov, N. S. Struchkov, D. Y. Nefedov, A. O. Antonenko, P. Cai, Z. Liu, P. N. Brunkov, *Adv. Mater. Technol.* **2022**, *7*, 2101250.
[34] F. Rigoni, S. Freddi, S. Pagliara, G. Drera, L. Sangaletti, J. M. Suisse, M. Bouvet, A. M. Malovichko, A. V. Emelianov, I. I. Bobrinetskiy, *Nanotechnology* **2017**, *28*, 255502.
[35] L. Zhang, F. Tian, D. Zhang, *Electronic Nose: Algorithmic Challenges*, Springer Nature, Singapore **2018**.
[36] S. Freddi, D. Perilli, L. Vaghi, M. Monti, A. Papagni, C. Di Valentin, L. Sangaletti, *ACS Nano* **2022**, *16*, 10456.
[37] O. Shaham, L. Carmel, D. Harel, *Sens. Actuators B Chem.* **2005**, *106*, 76.
[38] D. Li, Y. Shao, Q. Zhang, M. Qu, J. Ping, Y. Fu, J. Xie, *Analyst* **2021**, *146*, 5704.
[39] Y. J. Hwang, H. Yu, G. Lee, I. Shackery, J. Seong, Y. Jung, S.-H. Sung, J. Choi, S. C. Jun, *Microsyst. Nanoeng.* **2023**, *9*, 28.
[40] N. S. S. Capman, X. V. Zhen, J. T. Nelson, V. R. S. Kumar Chaganti, R. C. Finc, M. J. Lyden, T. L. Williams, M. Freking, G. J. Sherwood, P. Bühlmann, C. J. Hogan, S. J. Koester, *ACS Nano* **2022**, *16*, 19567.
[41] A. Lipatov, A. Varezhnikov, P. Wilson, V. Sysoev, A. Kolmakov, A. Sinitskii, *Nanoscale* **2013**, *5*, 5426.
[42] U. N. Thakur, R. Bhardwaj, P. K. Ajmera, A. Hazra, *Eng. Res. Express* **2022**, *4*, 025008.
[43] C. Homma, M. Tsukiiwa, H. Noguchi, M. Tanaka, M. Okochi, H. Tomizawa, Y. Sugizaki, A. Isobayashi, Y. Hayamizu, *Biosens. Bioelectron.* **2023**, *224*, 115047.
[44] U. N. Thakur, A. Hazra, *Measurement* **2023**, *222*, 113593.
[45] A. Piras, C. Ehlert, G. Gryn'ova, W. Interdiscip, *Rev. Comput. Mol. Sci.* **2021**, *11*, e1526.
[46] X. Tang, M. Debliquy, D. Lahem, Y. Yan, J. P. Raskin, *Sensors* **2021**, *21*, 1443.
[47] J. H. Gosling, O. Makarovsky, F. Wang, N. D. Cottam, M. T. Greenaway, A. Patanè, R. D. Wildman, C. J. Tuck, L. Turyanska, T. M. Fromhold, *Commun. Phys.* **2021**, *4*, 30.
[48] G. Drera, G. Salvinelli, J. Åhlund, P. G. Karlsson, B. Wannberg, E. Magnano, S. Nappini, L. Sangaletti, *J. Electron Spectrosc. Relat. Phenom.* **2014**, *195*, 109.
[49] A. F. Agarap, *arXiv* **2018**, ArXiv 1803 08375.
[50] B. Asadi, H. Jiang, *arXiv* **2020**, ArXiv 2002.04060.
[51] S. R. Dubey, S. K. Singh, B. B. Chaudhuri, *Neurocomputing* **2022**, *503*, 92.
[52] A. K. Dubey, V. Jain, in *Applications of Computing, Automation and Wireless Systems in Electrical Engineering*, (Eds.: S. Mishra, Y. Sood, A. Tomar), *553*, Springer, Singapore **2019**.